

Droplet morphology-based wettability tuning and design of fog harvesting mesh to minimize mesh-clogging

Arani Mukhopadhyay^{1†}, Arkadeep Datta[†], Partha Sarathi Dutta¹, Amitava Datta, Ranjan Ganguly*

Advanced Materials Research and Applications (AMRA) Laboratory
Department of Power Engineering, Jadavpur University, Kolkata-700106, India

[†]These authors contributed equally

*Corresponding author email: ranjan.ganguly@jadavpuruniversity.in

Abstract:

Fog harvesting relies on intercepting atmospheric or industrial fog by placing a porous obstacle, e.g., a mesh and collecting the deposited water. In the face of global water scarcity, such fog harvesting has emerged as a viable alternative source of potable water. Typical fog harvesting meshes suffer from poor collection efficiency due to aerodynamic bypassing of the oncoming fog stream and poor collection of the deposited water from the mesh. One pestering challenge in this context is the frequent clogging up of mesh pores by the deposited fog water, which not only yields low drainage efficiency but also generates high aerodynamic resistance to the oncoming fog stream, thereby negatively impacting the fog collection efficiency. Minimizing the clogging is possible by rendering the mesh fiber superhydrophobic, but that entails other detrimental effects like premature dripping and flow-induced re-entrainment of water droplets into the fog stream from the mesh fiber. Herein, we improvise on the traditional interweaved metal mesh designs by defining critical parameters, viz., mesh pitch, shade coefficient, and fiber wettability, and deduce their optimal values from numerically and experimentally observed morphology of collected fog-water droplets under various operating scenarios. We extend our investigations over a varying range of mesh-wettability, including superhydrophilic and hydrophobic fibers, and go on to find optimal shade coefficients which would theoretically render *clog-proof* fog harvesting meshes. The aerodynamic, deposition, and overall collection efficiencies are characterized. Hydrophobic meshes with square pores, having fiber diameters smaller than the capillary length scale of water, and an optimal shade coefficient, are found to be the most effective design of such *clog-proof* meshes.

Keywords: *Fog harvesting; Droplet morphology; Droplet detachment; Wettability engineering; Surface Evolver; Fog harvesting mesh design; optimization; efficiency*

1 Introduction

The accentuating crisis of freshwater in the last few decades has led to a serious drive for development of technology focused on sustainable water harvesting [1]. Harvesting fog from atmospheric [2] and industrial sources [3] have emerged as an affordable and viable alternative. A fog-laden stream passing through a mesh of metal or polypropylene fibers deposits droplets on the fibers by inertial impaction, physical interception, and Brownian diffusion [4]. Progressive deposition and droplet coalescence increases the liquid volume on the mesh, leading to the formation of droplets of different shapes. These droplets in turn interact with one another or with the neighboring mesh fibers to clog a mesh-pore either partially or completely, thereby offering greater hydrodynamic resistance to the oncoming fog stream, diminishing further fog droplet deposition. Such clogging of mesh pores can consequently reduce the aerodynamic and deposition efficiencies of the mesh and is prevalent in traditional interweaved metal meshes, as shown in Figure 1A. Mesh-clogging, which is strongly influenced by the fiber contact angle (Figure 1A inset), can theoretically be reduced by rendering the mesh fibers highly water-repellent (superhydrophobic) or by sufficient reduction of droplet adhesion via surface engineering [5]. However, this can accentuate the problem of droplet carryover or re-entrainment into the fog stream (see Figure 1B), which is caused by the aerodynamic drag on the deposited droplets on the fiber and is also influenced by the deposited droplet volume and morphology. Besides, as the liquid volume grows due to the successive deposition and coalescence of fog droplets on the mesh fibers, it tends to drip under the influence of gravity or slide down the mesh. The volume of the liquid droplet upon detachment from the fiber is an important parameter in this context [6]. While premature dripping of collected small droplets from the mesh into the open is both deterrent and detrimental for the collection (because the smaller droplets could easily get re-entrained into the fog stream), large droplets that adhere on to the mesh fibers have greater chances of clogging the entire pore and drastically reducing mesh efficiency [7]. Therefore, to maximize the collection efficiency, the fog droplets deposited on the fog net should slide down the mesh into a collector without either clogging the mesh pore or prematurely detaching from the mesh surface due to gravity (Figure 1B) [5]. The size and morphology of the droplet is a contributing factor that leads to clogging of mesh pores, wherein it provides aerodynamic resistance to the oncoming fog stream. Partial or complete clogging of mesh pores significantly impacts the mesh aerodynamic efficiency and reduces further deposition of fog droplets, thus affecting the deposition efficiency. It is therefore of utmost importance to have a clear understanding of the morphological evolution of a droplet on the mesh fiber ensuing from fog harvesting and pertinent parameters necessary in design of ‘*clog-proof*’ meshes.

A logical step to develop such an understanding of the behavior and morphology of deposited fog-water drops on a mesh is to deconstruct the mesh into its constituent cylindrical fibers and to focus on the interaction of a single droplet on such a fiber. Fog harvesting meshes, commonly utilized for collecting fog from diverse sources such as natural environments or industrial cooling towers, typically feature an arrangement of interwoven horizontal and vertical fibers. Vertical elements within these meshes play a pivotal role in facilitating the drainage of accumulated fog droplets [8], thus posing no threat related to clogging. In this context, Shi et al. [9, 10] and Goswami et al. [11] have underscored the effectiveness of harp-like mesh – the mesh has only an array of vertical elements – particularly in moderate fog conditions. However, the harp-design is found to be less viable in scenarios involving heavy fogging or tilted mesh arrangement (as one requires in cooling tower fog harvesters) due to their structural weaknesses and susceptibility to tangling [12]. Therefore, traditional interwoven meshes, incorporating both horizontal and vertical

components, have emerged as the optimal choice for effective fog harvesting in most applications. The horizontal fibers in such a mesh add to its structural rigidity. But, contrary to the vertical fiber elements, the horizontal fibers contribute to clogging and droplet drainage resistance [13]. Therefore, our study focuses on the accumulated fog water droplet size and morphology on a horizontal member of a fog-harvesting mesh. The droplet morphology in such a case would depend on the surface tension of the liquid-gas interface (water-air in this case), the deposited liquid volume, the fiber diameter, its orientation with respect to gravity, and the fiber-surface wettability.

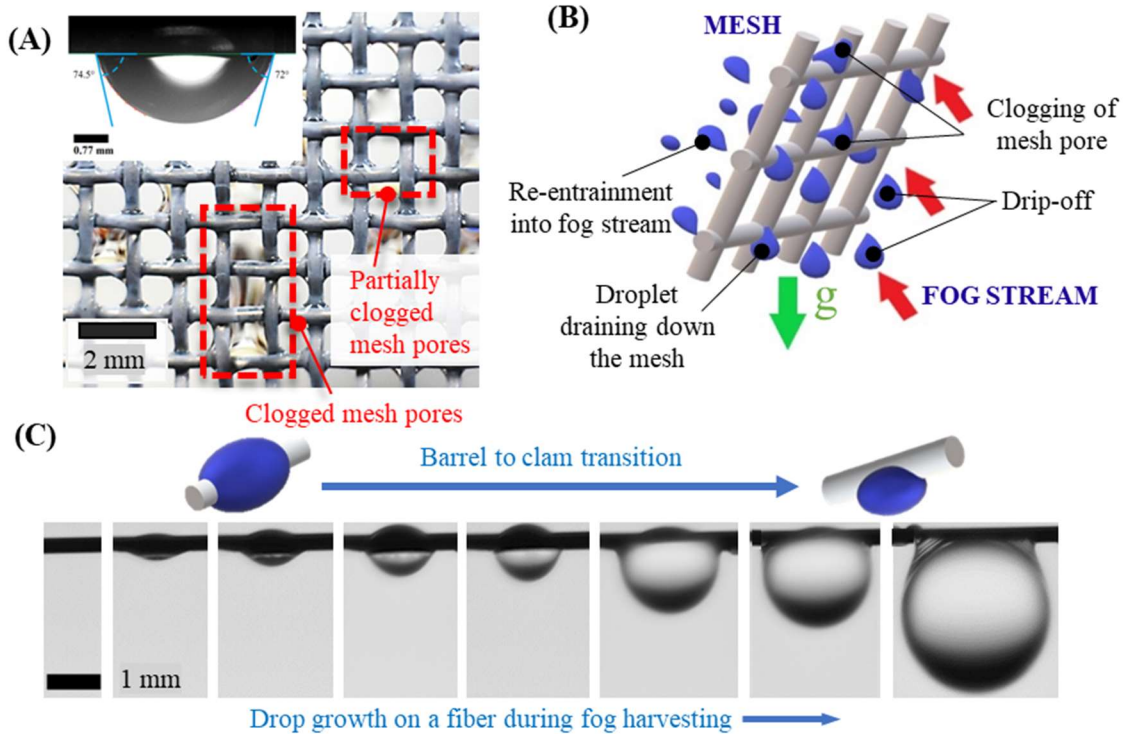


Figure 1: (A) Traditional interweaved metal meshes are prone to clogging of mesh pores. Mesh clogging has strong dependence on the contact angle of the fibers (inset). (B) Re-entrainment of collected droplets into the fog-stream and premature dripping of liquid droplets from a fog-harvester mesh affects collection. (C) A growing droplet on a thin fiber can undergo dramatic morphological variations: from axisymmetric barrel shaped droplets to clamshell shapes.

A drop on a fiber can primarily assume two stable morphologies viz., an axisymmetric barrel shape or an asymmetric clamshell shape (Figure 1C) [14]. For example, a barrel shape is energetically preferred in cases where liquid volume is high, and the sessile droplet contact angles (of the droplet on the fiber) are low. On the contrary, clamshell shapes are energetically stable at lower liquid volumes or for high sessile droplet contact angles [15]. However, in-between such regimes of absolute stability, there exist metastable regimes wherein both shapes emerge as energetically preferred. When a metastable barrel droplet is subjected to non-axisymmetric body-forces or disturbances, it changes to a clamshell shape, which enhances the chances of its detachment from the fiber. Carroll [16] examined the solution of the Laplace equation for excess pressure in a barrel-shaped axisymmetric droplet on a fiber and derived an analytical relation among the droplet profile, volume, and stability. McHale et al. [17] later took up this solution

along with numerical results for a clamshell shape while using a finite element approach to probe into inflection in droplet profile and stability. Factors like diameter and surface chemistry of the underlying fiber significantly influence the wetting properties, thereby playing a strong influence on the final droplet morphology on the fiber [6, 18]. For example, decreasing the reduced volume ($V_R = V/(r_f)^3$, where r_f = the fiber radius and V = the volume of the fiber-attached droplet) or increasing the contact angle results in a “roll-up” of the barrel to clamshell shape [17]. The dependence of the roll-up process on wettability and reduced volume under negligible gravitational influence was further extensively studied by utilizing functionalized fibers for observing the transition volumes between the barrel and clamshell shapes [15]. It was seen that under low fiber Bond number ($Bo = \rho g r_f^2 / \gamma$, where r_f = the fiber radius, ρ = liquid density, g = acceleration due to gravity, and γ = surface tension at the air-water interface) scenarios, droplets can exist mainly in three regimes, viz., the two absolute-stability regimes (for barrel and clamshell shapes) and the coexistence (or meta-stability) regime wherein both these shapes are independently stable [19]. However certain technological applications require knowledge of droplet shapes when gravity is more pronounced and this scenario was taken up by Chou et al. [20], who showed that droplets exist primarily in three regimes which include downward clamshell shapes, an independent coexistence regime and falling off, wherein the droplet detaches from the fiber.

To better understand the role of droplet morphology during fog harvesting, particularly its role to accentuate mesh-clogging, we numerically estimated droplet morphology transition regimes, i.e., from barrels to clamshells and vice versa, via the use of a finite element Surface Evolver package [21]. Morphological parameters from the developed droplet morphology were then used to estimate fog-harvesting mesh geometry pertaining to the best shade coefficient (SC) (defined as the fraction of the projected mesh area that is obstructed by the solid fibers of the mesh) for designing meshes that should never clog. To further simplify this problem, we assumed meshes with only symmetric square pores, being built from atomically smooth cylindrical fibers with no roughness. While a significant volume of literature has been dedicated in deployment of flat solid surfaces embellished with 3-D features like cascading patterns [22], bumps [23] or bio-inspired surface modifications [24, 25, 26], it is important to note that such flat plates suffer from significant aerodynamic bypassing at practical length scales (i.e., the fog stream gets diverted by the aerodynamic resistance offered by a large flat plate in its path, leading to very little fog deposition). Moreover, the micro/nano-scale surface embellishments, despite showing attractive droplet drainage features at the laboratory scale, lack scalability for mass production in industrial or community fog harvesting applications [27, 28]. Heavy fogging under high stream velocity, as is typical in industrial application scenarios, calls for sturdier meshes that are suited for long term use [7]. Taking all such factors into account, we argue that mass producible interwoven metal meshes (having geometry depicted in Figure 1A) are best suited for such applications. However, such meshes have been reported to suffer from serious clogging issues [29] and their design needs to be optimized for better fog harvesting. While there have been multiple studies dedicated to the development of novel mesh designs or suitable surface modifications [30, 31], almost none have investigated into understanding the mesh geometry parameters and droplet morphology interactions that lead to clogging. Herein, we attempt to theoretically design the salient fog harvesting mesh parameters, viz., the fiber diameter and intra-fiber spacing, by drawing heavily from droplet morphology, such that a sessile droplet on a fiber does not interact with the neighboring mesh fibers thereby ensuring a *clog-proof* design. Thereafter, critical shade coefficients for such *clog-proof* fog harvesting meshes, constituting of ideal cylindrical fibers interweaved to form square mesh pores, have been specified, and their aerodynamic properties,

and deposition efficiencies have been estimated. To further generalize our theory, such investigations carried out numerically with the help of Surface Evolver (SE) [21], have also been experimentally validated over a wide range of wettability for both superhydrophilic and hydrophobic fibers.

2 Methodology

As already mentioned, a drop on the fiber of a fog harvesting mesh grows by consequent droplet coalescence and fog deposition, wherein it can assume either an axisymmetric barrel shape or an asymmetric clamshell shape (see Figure 1C) depending on its V_R and Bo . As the droplet grows, its weight can overcome the adhesion force between the droplet and the mesh fiber, after which it detaches. However, there is another possibility: the droplet may stretch transversely or laterally to reach neighboring mesh fibers and form capillary bridges, thereby leading to an increase of surface adhesion force and preventing detachment. A droplet interacting with more than one fiber can therefore acquire larger volumes before it would detach [32], and hence accentuate the chance of clogging up the mesh pore. This would not only reduce the intended drainage of the collected fog-water (into the designated collector) but also increase aerodynamic resistance, thereby reducing total mesh efficiency. The wettability of the mesh fibers, represented by its contact angle (θ), plays a strong role in determining the droplet morphology and whether it will clog the mesh under standard operation scenarios [29]. We investigate the droplet morphologies arising during fog harvesting, both experimentally and numerically, and identify the optimal design to avoid the formation of such clogging. Effects of varying fiber diameter and wettability conditions were also characterized to arrive at the design of *clog-proof* meshes.

2.1 Experimental

Experiments were carried out to characterize the morphology of water droplets on horizontally mounted mesh fibers through direct imaging. Fibers of three different wettability, viz., untreated fibers (control), superhydrophilic (SHPL), and hydrophobic (HPB) were chosen. For the control surfaces, stainless steel fibers (SS-304), with measured roughness (R_a) $\sim 0.29 \pm 0.11$ μm and outer diameters varying from 0.25 – 6 mm were used to mimic the fibers of a fog harvesting mesh. The fiber diameters were measured with a digital screw gauge (Yuzuki, least count of 0.001 mm). All surface roughness measurements were carried out using a contact stylus profilometer (Landtek Instruments). All the fibers were cleansed via bath sonication (PCI Analytics), first in acetone and then in distilled water for 10 minutes. Thereafter, contact angle (θ) measurements were performed using an optical goniometer (Holmarc), for sessile droplets in the clamshell shape, as depicted earlier in Figure 1A (inset). Smooth aluminum cylinders of outer diameter 2 – 6 mm and $\theta \sim 71^\circ \pm 3^\circ$ were turned SHPL by sandblasting, followed by etching in 3N hydrochloric acid (HCl) solution which creates micro-nano roughness on the surface. The SHPL surfaces were then passivated in boiling water for 30 minutes thereby creating stable hierarchical böhmite structures [33]. The fibers displayed a very low θ ($< 5^\circ$) with a roughness of $R_a \sim 4.01 \pm 0.22$ μm [34]. The control fibers were turned HPB ($\theta \sim 104^\circ \pm 3^\circ$, measured roughness, $R_a \sim 0.58 \pm 0.31$ μm) by dip-coating with polydimethylsiloxane (PDMS): fibers were first ultrasonicated in acetone and water, dried and then dip-coated (NXT dip-KPM, Apex Instruments) in a PDMS solution (SYLGARD™ 184 Silicone Elastomer, Dow; premixed thoroughly with a crosslinking agent at a ratio of 10:1 by weight) at an axial draw-out velocity of 10 mm/s. The coated fibers were then cured in a hot-air convection oven at 120 °C for ~ 2 hours.

An experimental setup as shown in Figure 2A was developed for obtaining the droplet morphology and dimensions through direct imaging. A horizontally positioned three jaw chuck was used to firmly hold onto the wettability engineered cylindrical fibers. A flicker-free LED-powered (LT Max, GSVitec) white screen was used as a background for all imaging purposes. Live feed from a digital camera (Nikon D7200, with Nikkor AF-SDX 50 mm lens, mounted on 12 – 36 mm extension tubes) was stored onto a computer and viewed simultaneously on a monitor during experimentation. A micropipette (Thermo Scientific) was used to gently dispense liquid volumes on top of the fibers (see Figure 2B) in quanta of $V_{LD} = 1.0 \mu\text{L}$ (the least count of the dispenser).

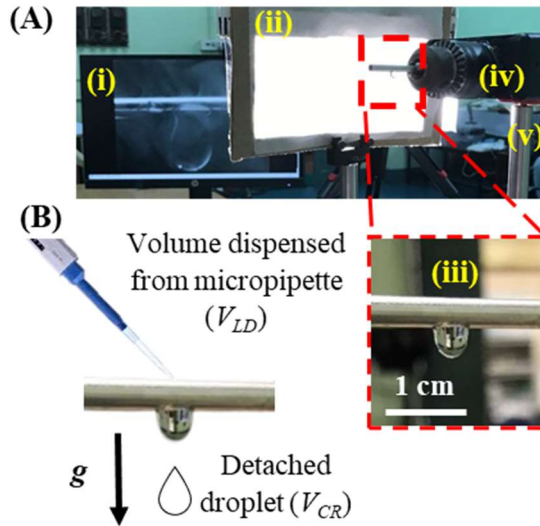


Figure 2 (A) Experimental setup with a computer display (i) and an illuminated white background (ii) to capture droplet morphology on a wettability-engineered metal fiber (iii, the zoomed-in section). The metal fiber was held by a horizontally placed three-way chuck (iv), which in turn was affixed to a firm stand (v). (B) Schematic of the arrangement for droplet volume addition using a micropipette. The volume was incremented, in steps of the least dispensable volume (V_{LD}) of the micropipette, until the droplet detached at V_{CR} .

After each droplet had coalesced with the previously deposited droplet, images were recorded, and the process of dispensing another droplet was repeated until the accumulated droplet detached from the fiber; the corresponding volume was termed as the critical volume of droplet detachment (V_{CR}). Care was taken while dispensing the droplet, such that the pipette tip did not touch the fiber – the droplets were dispensed with minimum disturbance to the fiber – to avoid any external perturbations (e.g., wind shear, vibrations, etc.) and to minimize any unwanted dynamic behavior leading to droplet detachment. This technique is in-line with previously reported approaches adopted to replicate liquid deposition from fog impingement [35, 36].

2.2 Simulation

It is well known in the field of capillarity that a liquid bounded by a curved surface experiences an excess pressure, known as the Laplace pressure. Under conditions involving very low Bo , the Laplace excess pressure Δp , uniform throughout the drop, is given by

$$\Delta p = (p - p_0) = \gamma_{LV} \left(\frac{1}{R_1} + \frac{1}{R_2} \right) \quad (1)$$

where $(p - p_0)$ is the gauge pressure within the droplet, γ_{LV} the liquid surface tension and R_1 and R_2 are the principal radii of curvature of the droplet. For a droplet on a smooth fiber existing in an axisymmetric shape, this equation has been used for analytically expressing the droplet morphology using elliptic integrals by Carroll [16] to determine relevant quantities pertaining to barrel droplet geometry. However, no such exact solution exists if the axial symmetry breaks down, for example, in cases when the effect of gravity is more prevalent, or if the droplet assumes a clamshell shape, or if both happens. For such a general case, the equilibrium behavior of the free gas-liquid interface (expressed implicitly as $F = f(x, y, z)$) of the droplet, on a smooth, solid cylindrical surface (expressed implicitly as $S = s(x, y, z)$) is dictated by the Young-Laplace equation [37, 38]. This equation relates to the Laplace pressure Δp (the pressure difference across the liquid interface) with the mean curvature κ_m of the interface, the gravity (g) and the surface tension (γ_{LV}) as,

$$2\gamma_{LV}\kappa_m = \Delta p - \Delta\rho\vec{g} \cdot \vec{z} \quad (2)$$

Where $\Delta\rho$ denotes the density difference between the liquid and the gas and z is the local elevation of the surface (from any arbitrarily chosen datum). Similar theoretical modelling had been implemented by Ray and Ganguly [39], for evolution of nano-liter droplets on micro-pillared surfaces, and by Datta et al. [6] in estimation of detachment volumes from cylindrical fibers. These solutions are constrained by the imposition of two boundary conditions (BCs) as depicted in Equations 3a and 3b, wherein the first BC (BC 1: Eq. 3a) represents the liquid-solid contact on the cylindrically curved, smooth surface of the wire, while the second BC (BC 2: Eq. 3b) specifies the surface wettability in terms of the contact angle θ and \vec{n}_S (the normal to the surface S).

$$\text{BC 1: } \mathbf{F}(\mathbf{S}) = \mathbf{0} \text{ where } \mathbf{S}(x, y, z) = 0 \quad (3a)$$

$$\text{BC 2: } \nabla F \cdot \vec{n}_S = |\nabla F| \sin \theta \text{ on } S(x, y, z) = 0 \quad (3b)$$

Herein, the problem requires resolving the Laplace equation and the surface morphology in three-dimensions for the clamshell geometry, which warrants the use of numerical simulations, e.g., using a standard surface evolver software. Surface Evolver (SE) is an open access finite element package that moves triangulated surfaces in an iterative procedure to minimize a user-defined total energy function for a described geometry via a gradient search algorithm [21]. User input comprises of an initial geometry along with boundary constraints and energy integrals defined over the surface or volume. Simulations start with an arbitrary geometry (e.g., prismatic) shape of liquid volume on the cylindrical wire. Choice of the initial disposition of this liquid volume (e.g., encompassing the cylinder, akin to the barrel morphology, or one-sided, akin to the clamshell morphology) has been made carefully to ensure convergence. With the passage of iterations, the shape of the liquid volume evolves to minimize the total energy of the droplet (surface + gravitational potential). Each iteration towards the solution moves through intermediate surface morphologies which do not necessarily correlate with the physical shape of the droplet, and at the end, the shape where no significant decrease of energy after subsequent iteration is observed is considered as the final morphology [39]. Detailed explanation on the approach adopted in the SE simulation to arrive at droplet morphologies has been provided in the Electronic Supplementary Information (ESI) Section S1.0. In the event of small Bo (e.g., when gravity is negligible, or the droplet size is small), the total free energy of a drop is mainly dependent on the interfacial surface energies and is described by Equation 4.

$$E_{free} = \gamma_{LV}A_{LV} + (\gamma_{SL} - \gamma_{SV})A_{SL} \quad (4)$$

However, in cases of higher Bond numbers, Equation 4 is modified with a volume integral to account for the presence of gravitational energy. Using Young's equation to relate to the contact angle, we can rewrite Equation 4 as follows,

$$E_{free} = \gamma_{LV}(A_{LV} - A_{SL} \cos \theta) + \rho g \iiint_V z dV \quad (5)$$

The results from the ensuing simulations were compared to pre-existing data in the literature, and against Carroll's analytical expression for barrel-to-clam transitions [40]. The versatility of the SE code is captured from the capability to model such transition phenomena. The adaptive grid mesh refinement criterion and the convergence criterion have been elucidated in the Electronic Supplementary Information (ESI) Sections S1.1 and S1.2. Thereafter, the developed code was extended to accommodate for variations in wire Bond number (Bo) arising from a change of fiber diameter or due to the gravitational influence. Hence, parametric variations were carried out to identify the conditions of the morphology transition for varying Bo scenario. For all simulations, interactions between smooth horizontal cylindrical fibers with pure water ($\gamma_{LV} = 72$ mN/m) were considered. The minimum volume considered for observing the droplet morphology transition in SE was of the order of 0.1 μ L. Therefore, effects of line tension prevalent for nanoscopic droplets can be safely neglected at such scales [41].

3 Results and Discussions

3.1 Barrel or Clam?

3.1.1 Surface Evolver (SE) simulations

To ascertain the regimes of droplet absolute and meta-stability and its dependence on V_R and θ , simulations were carried out in SE for drop-on-fiber systems for fixed r_f (corresponding to fixed wire Bo). For this purpose, an arbitrary volume of the drop was chosen, in any fixed geometry pertaining to either a stable barrel or clamshell shape. Thereafter, simulations were repeated with an increment or decrement of θ in steps of 1° until the drop morphed into another stable geometry, or got detached from the fiber. A sequence of such simulations has been shown in Figure 3A, where the contact angle was incremented for fixed V_R and wire Bo and a transformation of the droplet from a barrel shape to a stable asymmetric clamshell shape was observed.

To demarcate the absolute stability regimes in barrel shape at a fixed V_R and fiber Bo , SE simulations were carried out for stable clamshell droplets which appeared at relatively higher liquid-fiber contact angle $\theta (> 30^\circ)$. Thereafter, the simulations were repeated with θ continually decreasing in steps of 1° to arrive at a final morphology wherein clamshell-shaped drops would no longer be stable, and the drop would morph into a barrel shape. This transition marked the beginning of the absolute stability of the axisymmetric barrel shapes. All such transition points, wherein the drop morphs from a metastable clamshell into a stable barrel shape have been plotted in Figure 3B. Therefore, any drop-on-fiber system located to the left of the stability regimes shown in Figure 3B must be in the absolute barrel shape, whereas drops to the right represents a metastable clamshell/barrel shape regime (i.e., both barrel and clamshell shapes are energetically feasible). Furthermore, with an increase in fiber Bo (or increasing gravitational influence), the absolute stability regime in the barrel shape shifts leftward on the $V_R - \theta$ plane, indicating that greater surface tension forces would be required to maintain a stable barrel shape (Figure 3B). At greater fiber $Bo (\geq 0.0044)$ this regime is only present at very low contact angles ($\theta \leq 5^\circ$). Interestingly, it may be pointed out here that under idyllic scenarios and in the absence of any

perturbations/gravitational effects ($Bo = 0$) barrel shapes can grow indefinitely large. However, even the slightest gravitational effects or perturbations would morph it into an energetically preferred clamshell.

A similar methodology was implemented for establishing the absolute stability in clamshell regime for any particular fiber Bo . An axisymmetric barrel droplet of fixed V_R was first simulated on a fiber, after which the θ was incremented in steps of 1° until the droplet transitioned into an asymmetric clamshell. Thereafter, such simulations were extended for varying Bo to populate the morphology transition map diagram for stable clamshell geometry (Figure 3C). As explained earlier, any drop-on-fiber system to the left of such transition points would represent a metastable barrel/clamshell, whereas systems to the right of such transition curves represent absolute stability in the clamshell shape. Contrary to barrel shaped droplets, clamshell droplets are found to be energetically more favored for increasing wire Bo (increasing gravitational influence). An example case to illustrate this simulation methodology implemented in estimating absolute stability regimes for a drop-on-fiber system at a fiber Bo of 0.0002 is provided in the Electronic Supplementary Information (ESI) Section S1.2.

It is also interesting to note that, during an event of sustained droplet growth (e.g., via coalescence during fog harvesting or in condensation applications) or shrinkage (e.g., due to evaporation), the droplet shape can morph from one regime to the other (e.g., stable to meta-stable or vice versa), and then again back to the previous regime if the volume change continues further in the same direction (e.g., growth or shrinkage). Such phenomenon, termed as “re-entrant behavior” [15], has been highlighted both in Figures 3B and 3C with dashed lines. This behavior is observed during droplet growth on a surface having considerably low contact angles (θ) at higher fiber Bo . For example, if we consider the case of fiber $Bo = 0.0218$ in Figure 3C, the dashed line along $\theta \approx 15^\circ$ indicates that a droplet exhibiting a stable clamshell shape for $V_R < 40$ shifts to the meta-stable regime for a higher value of V_R , where it may also remain in a barrel shape (provided, however, it originated from a barrel shape). On further growth of the droplet, corresponding to $V_R > 140$, the droplet regains the absolute stability regime wherein only clamshells are energetically favored. A similar re-entrant behavior (meta-stable to stable-barrel, and then again to a meta-stable regime upon progressively increasing V_R) is also observed for the case of for fiber $Bo = 0.0044$ in Figure 3B, along the dashed line at $\theta \approx 4^\circ$. This behavior is an outgrowth of the simultaneous interplay of the gravitational potential energy and the surface energy of the fiber and the liquid.

Reckoning the morphological phase diagram constituted by Figures 3B and 3C is particularly relevant for the fog harvesting scenarios. In reality, the droplet would start to grow on the fiber from a very low value of V_R , which would engender a stable clamshell morphology (see Figure 3C). At larger values of V_R – the reduced volume increases progressively as the droplet grows because of subsequent fog deposition – the droplet morphology would be dictated both by the Bo and θ . Following observations of Figures 3B and 3C, the droplet would continue to remain in a clamshell morphology until the combination of Bo and θ encroaches in the stable barrel morphology regime. It may be noticed from Figure 3C that even for the thinnest fiber ($r_f = 0.25$ mm) investigated here (see Section 2.1), under normal gravitational ($g = 9.81$ m/s², corresponding Bo of 0.00212, which would lie on the right-hand side of the $Bo = 0.0044$ line) scenarios, a pendant clamshell morphology is always energetically preferred over an axisymmetric barrel (see Section S3.0 in ESI). Hence, in the following sections describing the experimental observations, and in further investigations for the design of *clog-proof* meshes, we limit our discussions only to clamshell shaped drops.

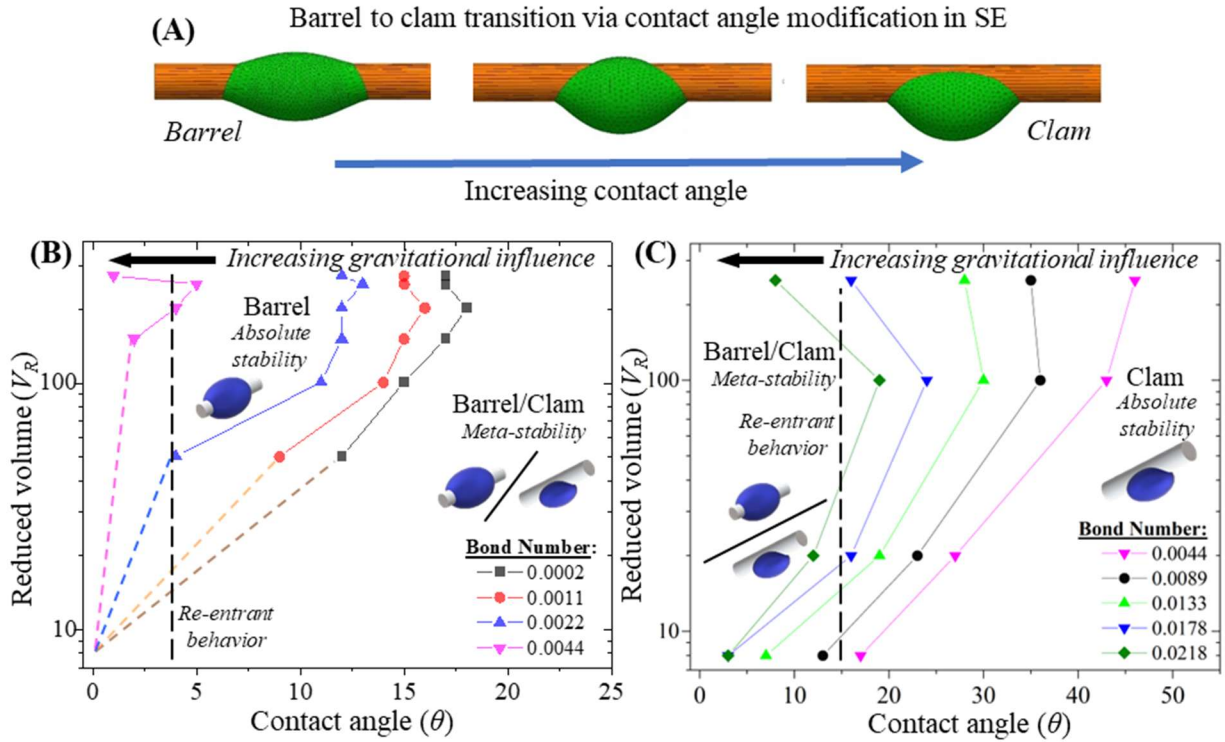


Figure 3: (A) Estimation of stable droplet morphology regimes from the SE simulations. Regime maps of droplet morphology on $V_R - \theta$ plane for different Bo : (B) lines demarcating the absolute barrel stability (left of each curve for the pertinent Bo) and barrel/clam metastable regimes; (C) lines demarcating the absolute clamshell stability (right of each curve for the pertinent Bo). Example cases of re-entrant behavior of the droplet from one stability regime to another and back have been marked with the dashed vertical lines in the regime plots.

3.1.2 Experimental investigations into droplet morphology

As explained earlier, experiments were undertaken on wettability engineered fibers to evaluate droplet morphologies and to attest to the simulation results obtained from SE. A series of images to capture the droplet growth on varying fiber diameters have been provided in Figure 4. It was observed that there is significant difference in the droplet morphology for variations in fiber diameter or wettability. As is evident from Figure 4A, droplets on SHPL fibers had a greater lateral spread compared to their vertical extent, while droplets on HPB fibers had smaller contact areas. Such a morphology can be explained theoretically by taking the surface energies into consideration: SHPL fibers have greater surface energy, therefore sessile droplet geometries result in maximized contact area and vice versa. Furthermore, the extent of the droplet morphology was also limited by its critical volume of detachment (V_{CR}), wherein the droplet detached from the fiber. As the volume of the droplet is increased, the lateral extent of droplets on SHPL fibers kept on increasing till they reach a maximum, as opposed to their HPB counterparts (wherein, extension of the vertical hang is favored compared to the increase in contact area of the drop-on-fiber system, Section S1.3 in ESI). We characterize the change of such extents by describing morphological parameters and using them to characterize *clog-proof* meshes in the following sections.

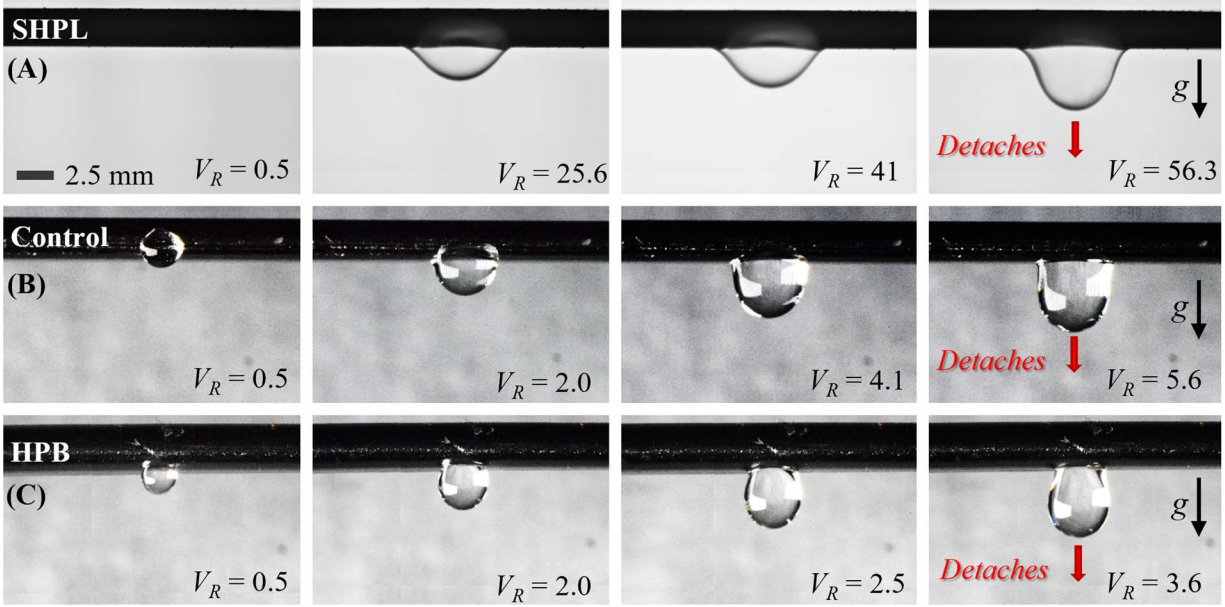


Figure 4: Clamshell droplet morphologies (for varying V_R) on wettability engineered fibers, as observed during experimentation. Droplets on SHPL fibers (A), were seen to spread laterally and had a greater lateral extent. Droplets on control fibers (untreated SS) showed no preference in change of lateral or vertical spread on increase of droplet volume (B), whereas droplets on HPB surfaces minimized their contact area while extending vertically with increase of volume (C). Comparisons between lateral and vertical extent of varying drop-on-fiber morphologies have been carried out in the next section. All experiments were carried out until the droplet reached the critical volume of detachment (V_{CR} , as seen in the last frame from each sequence), any volume addition after this would lead to droplet detachment. All images have the same scale bar, while each image show a fiber of diameter 2.7 mm.

Furthermore, for all the experimental trials conducted throughout this study, the control fiber ($\theta \approx 70^\circ$) diameters were varied from 0.25 mm to 6 mm, which corresponds to wire Bo of 0.00212 and 1.22625 [19]. Again, for experiments in the super-hydrophilic regime ($\theta < 5^\circ$), surface-treated aluminum fibers had diameter variations from 2 mm to 6 mm, corresponding to Bo variations from 0.13625 to 1.22625. From earlier stability regime plots in Figure 3, it is evident that for both these set of experiments, barrel shaped droplets would not be energetically preferred for any V_R . Similarly, barrel shaped droplets for fiber radii in the order of ~ 1 mm (corresponding Bo of 0.0340), in hydrophobic regimes ($\theta > 90^\circ$) are impossible under normal gravitational ($g = 9.81 \text{ m/s}^2$) scenarios. Therefore, and as explained earlier, realistic barrel-shaped droplets do not appear both during numerical simulations and in experimental investigations of collected droplets on fog harvesting meshes (Section S3.0 in ESI), and understanding morphologies of clamshell droplets hold key in design of *clog-proof* meshes.

3.2 Design and characterization of “clog-proof” meshes

3.2.1 Droplet maximal dimension

As evident from the SE simulations and the experiments described in the previous sections (refer to Figure 3A or Figure 4), a clamshell droplet growing on a cylindrical fiber extends its vertical hang (H) and its lateral spread (W , measured at the base or the girth of the droplet,

whichever was greater), until the droplet detaches from the fiber because of its weight. These characteristic dimensions have been described in Figure 5A, wherein the consistency between the experimentally observed and simulated droplet morphology have also been demonstrated for stainless steel control (SS 304, $\theta \sim 70^\circ$) fibers of diameter 1.27 mm (top image, droplet volume 10 μL , $V_R = 39.1$) and 4 mm (bottom image, droplet volume 45 μL , $V_R = 5.6$). It is seen from Figure 5A that the droplet hanging from the 1.27 mm fiber has $W > H$, while that from the 4 mm fiber exhibits $W < H$. It was also observed (See ESI Figure S3 B) that while H kept on increasing until detachment, the lateral spread only increased up to a certain maximum (W_{max}) and then decreases as the “detachment neck” forms in the droplet. Therefore, while H_{max} occurs just prior to the detachment (i.e., $V_R = V_{CR}$), W_{max} is observed at $V_R < V_{CR}$. Such a behavior ensues from the variation of the self-adjusting surface adhesion forces with the changing droplet footprint as it attempts to balance the gravitational influence on the droplet.

To examine the relative extents of H and W of a clamshell-shaped pendant droplet from the fiber, our SE simulations and experiments were further extended to describe the W and H values for different droplet-fiber contact angle and fiber diameters ($2r_f = 0.4, 1.27, 2.0, 4.0, 5.0$ and 6.0 mm, where r_f is the fiber radius). For SE simulations, droplet morphologies for varying $\theta = 15^\circ, 30^\circ, 70^\circ, 110^\circ$, and 160° were estimated, while for experiments the SHPL ($\theta < 5^\circ$), control ($\theta \sim 70^\circ$), and HPB ($\theta = 104^\circ$) surfaces were chosen. For both SE simulations and experiments, stable droplet morphologies and the corresponding H and W values were noted for different values of V_R – starting from zero to V_{CR} with incremental steps of V_{LD} . The largest values of W and H assumed by the droplet in the volume range ($0 \leq V_R \leq V_{CR}$) are recorded from each data set as W_{max} and H_{max} , respectively. The methodology of extracting the H_{max} and W_{max} from the SE simulation and the experimentally obtained images is elaborated in the ESI Section 1.3. These values of W_{max} and H_{max} , obtained over the entire parametric regime of θ and r_f are used to arrive at the fog harvesting mesh design criteria as described below.

As shown in Figure 5B, a droplet on the fiber of a mesh could always interact with its neighboring fibers to form capillary bridges, which would clog the mesh pore and impact fog capture adversely. Hence, for a given fiber radius of the mesh that has square-shaped pores, the pitch (distance between two fiber centerlines) needs to be greater than the maximal dimensions of the droplet spread or hang (viz., H_{max} and W_{max} respectively) to ensure that it never clogs. The underlying assumption is that the fog-water droplet grows symmetrically from a central point marked by the green arrows in Figure 5B. Although, in reality, fog droplets grow at multiple locations on the horizontal fiber of a mesh cell, but this assumption serves the purpose without eliciting much error because of a practically observed phenomenon. It was noticed from the experiments that fog-droplets growing asymmetrically, or near the corners of a mesh pore touches the nearest vertical fiber and drains down, leaving little chance of clogging the mesh pore. On the contrary, a droplet that grows from the middle of the mesh pore is at a greater risk of clogging the mesh pore as it will almost simultaneously touch vertical fibers on either side (Figure 5C and ESI Section S3.0). Therefore, we treat this configuration of fiber-attached droplet as the representative case to design clog-proof meshes.

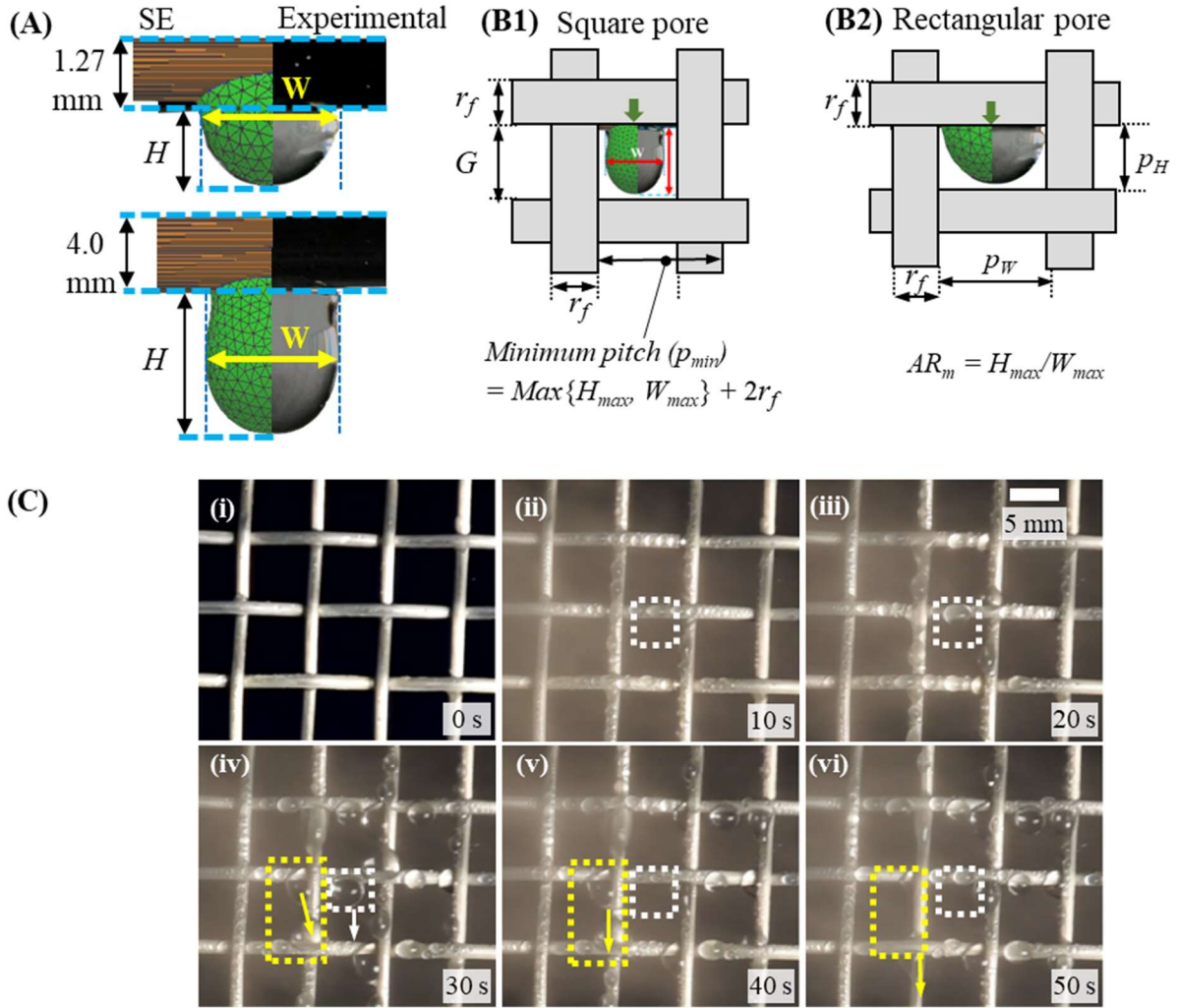


Figure 5: (A) Measurement of maximal width (W_{max}) and maximal vertical hang (H_{max}) in droplets hanging from 1.27 mm (top, droplet volume 10 μL) and 4 mm (bottom, droplet volume 45 μL) fibers (stainless steel 304, $\theta \sim 70^\circ$). Each figure comprises of two halves: the left half (colored in green) corresponds to SE simulations, while the other half is an experimental image. (B) Rationale for the design of *clog-proof* mesh with square pores (B1) and rectangular pores (B2): The mesh pitch should be such that a symmetrically growing droplet should not touch any other fiber, either on the side or at the bottom, as it grows until its detachment. The mesh pore dimensions, viz., the pore height and width have been marked as p_H and p_W respectively. (C) Fog droplets growing from the middle of the mesh pore has greater probability of clogging the mesh (marked in dashed white box), while droplets near a vertical fiber (marked in dashed yellow box) can drain down after contact with the nearest vertical fiber).

To further generalize the design of *clog-proof* fog harvesting meshes, both square and rectangular mesh pores have been considered. It is evident from Figure 5 B1 that the pitch (p) between the fibers for a square mesh is the sum of the mesh pore side (G , corresponding either of p_W or p_H for a square-pored mesh) and the fiber diameter, i.e.,

$$p = G + 2r_f \quad (6)$$

Once maximal droplet dimensions viz., H_{max} and W_{max} , had been evaluated for a specific combination of fiber radius and wettability, the minimum mesh pore dimensions $p_{min}(\theta, r_f)$ for a square-pore fog harvesting mesh were set equal to maximum of either H_{max} or W_{max} added to the mesh-fiber diameter, i.e.,

$$p_{min}(\theta, r_f) = \text{Max}\{H_{max}, W_{max}\} + 2r_f \quad (7)$$

This design approach for square-pored meshes would ensure that the droplet detaches before contacting any neighboring fibers. The maximal droplet dimension, evaluated for the first term on the right-hand side of Equation 7, is shown in Figure 6A as a function of the fiber diameter for different levels of fiber wettability as indicated by the respective assumed (for SE simulations) or measured (for experiments) contact angles.

For rectangular pore mesh designs (as previously illustrated in Figure 5 B2) the height- and width-wise dimensions, denoted as p_H and p_W , respectively, are not necessarily equal, and for designing such mesh, one should also keep in mind the aspect ratio (AR), i.e., the ratio of the height- and width-wise droplet dimensions. The AR estimated for the maximal dimensions of the droplet (for a particular fiber diameter and level of surface wettability), have been defined as the maximal aspect ratio and denoted as ($AR_m = H_{max}/W_{max}$). For a mesh with rectangular pores, the minimum value of the longer pitch (measured either height- or width-wise) should be linked with the maximal droplet dimension as

$$p_{min,longer}(\theta, r_f) = \text{Max}\{H_{max}, W_{max}\} + 2r_f, \quad (8a)$$

while the minimum value of the shorter pitch may be evaluated as

$$p_{min,shorter}(\theta, r_f) = \frac{\text{Max}\{H_{max}, W_{max}\}}{F} + 2r_f \quad (8b)$$

$$\begin{aligned} \text{where } F &= AR_m \quad \forall \{H_{max} > W_{max}\}; \\ &= 1/AR_m \quad \forall \{H_{max} < W_{max}\}; \text{ and} \\ &= 1 \quad \forall \{H_{max} = W_{max}\} \end{aligned} \quad (8c)$$

Therefore, for rectangular mesh design, both the droplet maximal dimension (i.e., $\text{Max}\{H_{max}, W_{max}\}$) and the droplet aspect ratio AR_m are needed to ascertain the minimum pitches in the two orthogonal directions. While the former is already available in Figure 6A, the AR_m values have been plotted in Figure 6B against different fiber radii and for different wettability levels. Furthermore, a series of images in Figure 6C (taken during the experiments) show this variation of AR , at V_{CR} , for droplets on unmodified stainless steel control fibers.

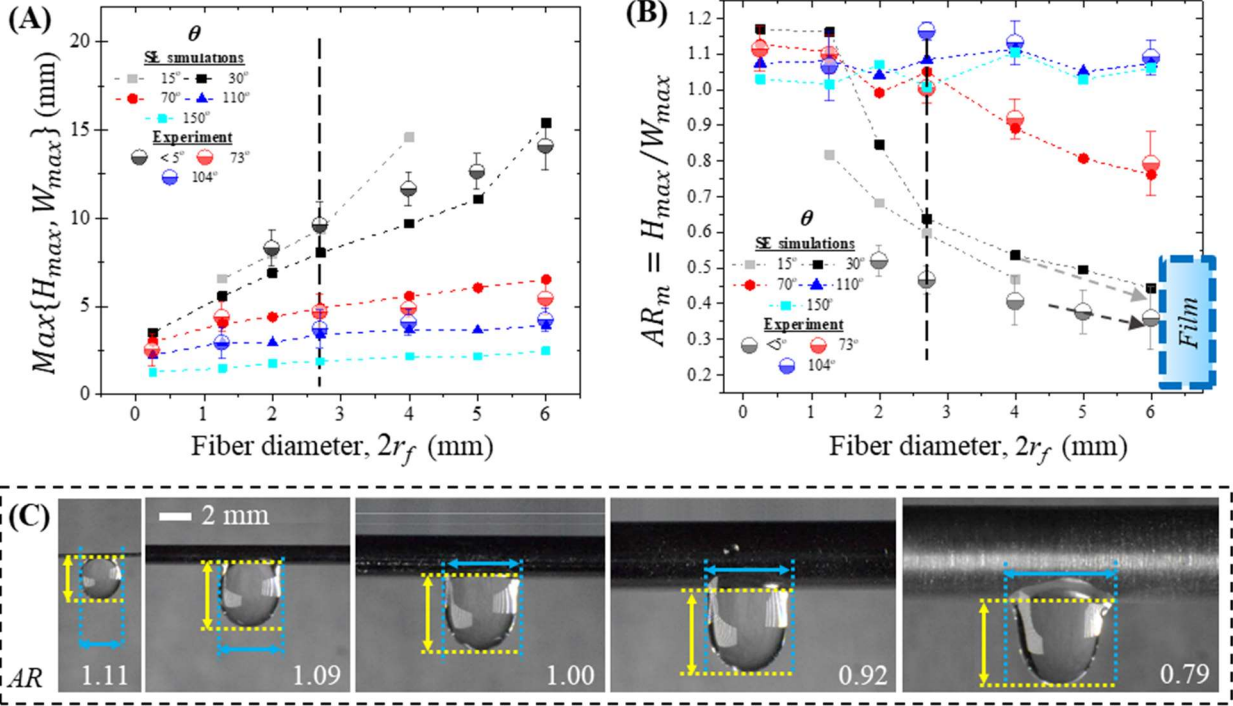


Figure 6: Variation of (A) the maximal droplet dimension ($Max\{H_{max}, W_{max}\}$) with the fiber radius, for the estimation of the minimum mesh pitch (as per Equation 7 or 8), and (B) the corresponding pore dimension maximal aspect ratio ($AR_m = H_{max}/W_{max}$, for the estimation of the minimum mesh pitch of a rectangular mesh as per Equation 8), plotted as functions of the fiber diameter for different mesh wettability. Legend: Filled symbols with dotted lines denote SE simulation results, half-filled circles denote the experimental data. Vertical dotted lines in both figures, mark the capillary length scale of water (~ 2.7 mm). (C) A series of experimental images showing the $AR=H/W$ calculated at the respective V_{CR} for different control fiber diameters ($\theta = 73^\circ$); H and W are marked in yellow and blue, respectively.

The maximal droplet dimension (Figure 6A) and droplet aspect ratio (Figure 6B) data show that both the SE simulations (filled symbols with dotted lines) and the experimental runs (half-filled circles) exhibit similar trend of variation with increasing r_f . The vertical dotted line in both the figures mark the capillary length scale of water (~ 2.7 mm). While the maximal droplet dimension (and hence the minimum mesh pitch length) is found to increase with the fiber diameter (Figure 6A), trends in variation of AR_m are seen to be different on either side of the capillary length scale. For fiber diameters smaller than the capillary length (i.e., on the left side of the dashed line in Figure 6B), AR_m is seen to converge near unity for a wide range of variation in wettability. This indicates that square shaped mesh pores are best suited for small fiber diameters. The final geometry of such *clog-proof* meshes would however depend on the wettability of the mesh fiber, and the *clog-proof* nature would rely on the minimum mesh pitch length as elucidated in Equations 7 and 8. Furthermore, for hydrophobic meshes, square mesh pores with appropriate minimum mesh pitch length appears to be *clog-proof*, since $AR_m \sim 1$ for almost all fiber diameters with $\theta = 110^\circ$ or 150° (from the SE simulations) and $\theta = 104^\circ$ (from the experimental measurements).

Therefore, it is evident from Figures 6A and 6B that the mesh-pore dimensions p_H and p_W are physical parameters entirely dependent on the drop-on-fiber morphology, the fiber diameter, and its wettability. While it is important in design of rectangular-pored *clog-proof* meshes, AR_m can also be interpreted as the ratio of the gravitational and surface-adhesion length scales acting on the droplet. A low AR_m (< 1.0) indicates greater lateral spread of the droplet throughout its growth (i.e., stronger influence of surface adhesion between the droplet and the fiber). On the other hand, a high AR_m (> 1.0) value will imply that the droplet-fiber contact width is less, and gravitational influence is more predominant. This interpretation is further invigorated by the fact that hydrophilic fibers ($\theta < 90^\circ$) are observed to have decreasing AR_m values with increasing fiber radii. The increasing lateral spread characterized by the decreasing AR_m is prominent from the experiments and simulations involving very low contact angles ($< 15^\circ$). For such highly wettable surfaces, an increase in fiber diameter sharply increases the maximal lateral spread (thus decreasing AR_m) and the droplet eventually spreads as a film, as indicated at the bottom right corner of the plots in Figure 6B. For SE simulations, runs with large fiber diameters (5 mm and 6 mm), did not to converge for very low contact angles ($\theta < 15^\circ$), as the droplet kept on spreading, forming a liquid film on the underside of the fiber. This observation also concurred with the experiments, where the contact line could no more be observed for superhydrophilic fibers, but the droplet would spread to form a film. We hypothesize that such film formation happens as capillary forces between the fiber and the droplet, at higher fiber diameter and lower contact angles, are sufficiently larger than gravitational forces and maximum energy minimization is obtained by assuming a film shaped morphology in place of a droplet. Our present study therefore excludes this film regime, since the mesh pitch dimensions, we intend to investigate here are in the millimetric range, which is at least an order of magnitude higher than the film thickness.

3.3 ‘Clog-proof’ mesh selection criteria and efficiencies

Once the droplet morphology parameters, necessary to define the geometry of *clog-proof* meshes, are determined and relevant mesh design parameters viz., r_f , p_H and p_W calculated, it becomes pertinent to evaluate the fog-collection performances of such optimally designed meshes. Furthermore, the estimation of fog harvesting mesh efficiencies require knowledge of shade coefficient, which depends on the fiber radius and the mesh pore geometry. The shade coefficient encompasses all parameters relevant to the mesh pore geometry, including the mesh pore aspect ratio (AR_m), and therefore estimation of mesh efficiencies can be carried out for all *clog-proof* meshes described herein. However, while the design criteria for both square-pore and rectangular-pore fog harvesting *clog-proof* mesh geometries have been specified earlier, only investigation of fog-capture performance of square-pored meshes have been taken up. The efficiencies of rectangular pored meshes can be evaluated in similar ways as described in the following sections.

As fog harvesting meshes intercept fog-laden wind, to collect droplets via subsequent deposition and coalescence on its fibers, it also offers a significant pressure drop to the flow. The deposited droplet eventually drains down the mesh for collection and later use. The total capture efficiency of such meshes are determined from the product of aerodynamic, deposition, and drainage efficiencies [3, 29]. We use the aerodynamic theory for the fog laden airflow through the mesh and the deposition dynamics of the fog droplets in the mesh that is designed for *clog-proof* operation following the minimum-pitch criteria described in the previous section. However, estimation of the drainage efficiency for such meshes is beyond the scope of the present study and may be taken up as a future exercise.

3.3.1 Aerodynamics of flow through a mesh

Fog capture meshes intercepting fog laden winds, present an interesting, but complicated flow over several bluff bodies, which causes a pressure drop across the mesh. The fluid dynamics of such an interception via a porous blunt mesh can be considered analogous to flow across a porous media, and modeled by considering three regions of interest during the flow as depicted in Figure 7A – *Region 1* wherein the upstream fog flow gets deflected owing to the obstruction imposed by the mesh in its path, *Region 2* denotes the location just after the net, while *Region 3* is located at the far downstream. As shown in Figure 7A, a stream tube (denoted by the blue-dotted lines) of cross section A_1 , smaller than the area A of the fog mesh, is defined to quantify the volume flow rate of the fog-laden flow through the mesh. Following the principle of continuity, for a fog stream approaching the mesh with free-stream velocity u , it can be shown that the cross-section areas A_1 and A are related with upstream velocity, u , and velocity of the fog-stream just after interaction with the mesh, w (as depicted in Figure 7A) as

$$A_1 u = A w \text{ or, } \frac{A_1}{A} = \frac{w}{u} = u^* \quad (9)$$

Here, u^* is defined as the “velocity ratio” for the given fog-flow conditions. For better estimation of the fog mesh aerodynamic efficiency, we resort to approximations as previously implemented by Koo [42] and Steiros [43]:

- Fog flow in region 1 is outside the stream tube encompassing the mesh and are inviscid and irrotational (potential flow approximations)
- In region 2, the fog flow follows the streamlines and is inviscid.
- Fog flow in region 3 is viscous, and characterized by significant mixing with the outer flow.
- There is significant mixing of the wake with outer flow in the interface between regions 2 and 3 which is independent of the induced velocity w .

The “fog interception ratio”, $\varphi = (A_1/A)$ (also referred in earlier studies as the “filtered fraction”) represents the fraction of the unperturbed flow reaching the mesh without getting diverted. From this, the aerodynamic efficiency (η_a , the fraction of the unperturbed oncoming flow which is directed toward the projected solid area of the mesh) can be estimated as by $\eta_a = \varphi \cdot SC$ where SC is the shade coefficient of the mesh [44]. Therefore, the aerodynamic efficiency can be expressed both as a function of the velocity ratio and the fog-interception ratio, by combining the definition of η_a with Equation 9, such that,

$$\eta_a = \frac{w}{u} SC = u^* \cdot SC = \varphi \cdot SC \quad (10)$$

Therefore, for estimation of the fog-interception ratio (φ), pressure drops at the microscale (for inviscid flows through a porous substrate) are compared with the resulting pressure drop at the macroscale arising due to interaction of the fog-stream with a blunt body (herein the fog-mesh) at higher Reynolds number [45]. This comparison leads to a direct definition of the fog-interception ratio (φ) as shown in Equation 11,

$$\varphi = \frac{w}{u} = u^* = \frac{A_1}{A} = \sqrt{\frac{C_D}{k}} \quad (11)$$

where C_D and k are the drag and pressure drop coefficients arising from the fluid mechanical analysis of the problem at the macroscale and the microscale approach to the problem respectively [45]. Furthermore, such coefficients in inviscid flows through a solid blunt porous body for potential flow approximations have been extensively explored in earlier research by Koo [42] and Steiros [43]. k and C_D are directly related to the velocity ratio (u^*) and the shade coefficient (SC) as expressed in equations 12 and 13, respectively.

$$k = \left(\frac{1}{(1-SC)^2} - 1 \right) - \frac{4}{3} \frac{(1-u^*)^3}{u^{*2}(2-u^*)^2} \quad (12)$$

$$C_D = \frac{4}{3} \frac{(1-u^*)(2+u^*)}{(2-u^*)} \quad (13)$$

Using equations 11 – 13, the velocity ratio can be implicitly solved for $SC \in [0,1]$, and may be expressed as a function of the shade coefficient or, $u^* = f(SC)$, using a linear regression fit (Equation 13a). This explicit form may, in turn, be used to estimate the aerodynamic efficiency as a function of SC in a fog harvesting mesh (Equation 13b).

$$u^* = 1.09 - 1.05SC, \quad R^2 = 0.99 \quad (13a)$$

$$\eta_a = 1.09SC - 1.05SC^2 \quad (13b)$$

Figure 7B shows the aerodynamic efficiency of square-pore fog harvesting meshes of varying fiber diameter and wettability, wherein the SC was chosen using the criteria of minimum mesh pitch $p_{min}(\theta, r_f)$ based on the maximal droplet dimensions (Figure 6A), to realize the *clog-proof* nature of the mesh. Therefore, for a given fiber diameter and wettability,

$$SC = \left[1 - \frac{2r_f}{p_{min}(\theta, r_f)} \right]^2 \quad (14)$$

Each curve for *clog-proof* mesh SC in Figure 7B – drawn at a specified wettability values – divides the graph into two regions. The region upwards of each curve (i.e., at a greater SC , implying that the mesh pitch for a given fiber diameter is smaller than that obtained from Equation 7) indicates a regions of mesh design prone to clogging. Whereas the region below the optimal SC curve implies that the mesh pitch is larger than the limit set by Equation 7, and hence the mesh will remain clog-free. To describe the overall performance of the mesh, both in terms of its aerodynamic efficiency and ability to avoid clogging, Figure 7B is also shaded with the color map contours of aerodynamic efficiencies, as computed from Equation 13b. For better clarity, the aerodynamic efficiency - SC curve is also shown by the side in Figure 7B(ii), wherein the aerodynamic efficiency is seen to peak ($\eta_{a,max} = 28.31\%$) at an optimum of $SC_{opt} = 0.52$.

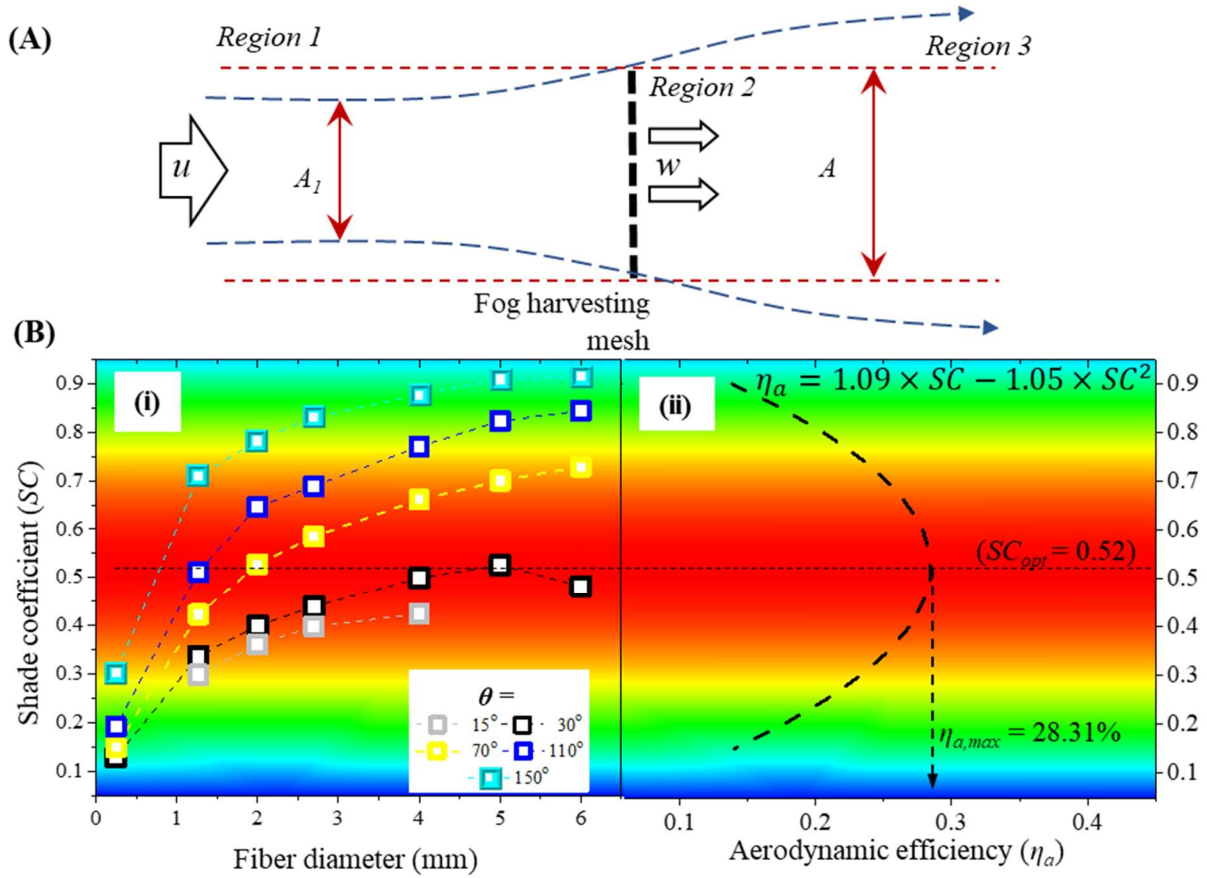


Figure 7: (A) Schematic of flow through a mesh placed in the path of fog laden wind. (after Steiros [43]). Flow in *Region 1* deviates and goes around the mesh; fog within the upstream cross-sectional area A_1 (less than the projected mesh area) interacts with the fog mesh. *Region 2* occurs just after the mesh, while *Region 3* is located at far downwind where mixing of flows from *Regions 1* and *2* occur. (B-i) Variation of the *clog-proof* SC values with the mesh fiber diameter for different fiber wettability. The *clog-proof* SC is calculated corresponding to the minimum mesh pitch lengths for square-pore fog meshes as suggested in Figure 6A. Regions above each curve (corresponding to a greater SC for a particular fiber diameter and wettability) are prone to clogging. Background color map denotes the corresponding aerodynamic efficiency as evaluated from (B-ii), which describes the variation of aerodynamic efficiency (also the black dashed curve) with the SC for square-pore fog-harvesting meshes. The color map background in (B-ii) is the same as that in (B-i), for easy comparison of η_a with *clog-proof* SC s.

Figure 7 indicates that, besides keeping the mesh design *clog-proof*, it is further possible to optimize the mesh geometry to maximize the aerodynamic efficiency close to the aforementioned value of $\eta_{a,max}$. This is illustrated in Figure 8A by showing the *clog-proof* design regimes of mesh fibers of three representative wettabilities (viz., $\theta = 30^\circ$, 70° and 150°) on the SC vs fiber diameter plane. The shaded regions (cross-hatched in respective colors) below each curve designate the design regime of *clog-proof* operation, while unshaded parts above the curves denote regimes of potential clogging. The rationale of mesh design would, therefore, be to remain within the shaded

region (of the respective mesh-wettability), and have SC as close as possible to $SC_{opt} = 0.52$. It may be seen from Figure 8A that a highly hydrophobic ($\theta=150^\circ$) mesh, which has a relatively smaller $p_{min}(\theta, r_f)$ may be designed as *clog-free* and also with $SC = SC_{opt} (= 0.52)$ for any fiber diameter greater than 0.8 mm. Therefore, the mesh is expected to remain clog-free and yield $\eta_{a,max} = 28.31\%$ for $2r_f > 0.8$ mm. For thinner fibers (i.e., $2r_f < 0.8$ mm), the maximum allowable SC for clog-proof operation will have to be lower, and hence the efficiency will be lower than $\eta_{a,max}$. For fibers with $\theta=70^\circ$, only meshes having $2r_f > 2.0$ mm may be designed with the optimum SC . Similarly, for a wettable mesh ($\theta=30^\circ$), $p_{min}(\theta, r_f)$ is much larger, and only meshes having $2r_f \sim 5$ mm can be designed with $SC = SC_{opt}$. Therefore, the corresponding plots of maximum achievable η_a values of the *clog-proof* meshes of different fiber diameters and for varying levels of fiber-wettability have been shown in Figure 8B. It is imperative from Figure 8B that η_a increases with the fiber diameter and attains $\eta_{a,max}$ beyond a certain value. It also transpires from Figure 8B that with smaller fiber diameter meshes, it is better to have a hydrophobic mesh to maintain both the attributes of high aerodynamic efficiency and *clog-proof* nature.

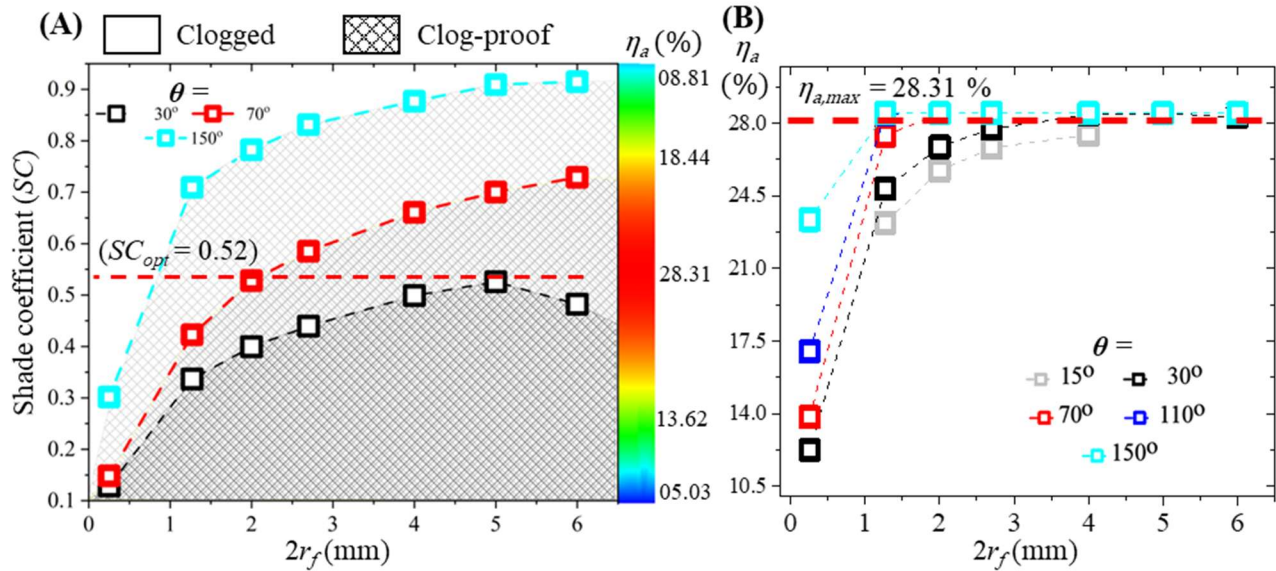


Figure 8: (A) Optimal shade coefficients for varying fiber diameter and wettability. The optimal mesh SC is calculated corresponding to *clog-proof* mesh pitch lengths from Figure 6A. Regions above each curve (for a specific level of fiber wettability) are prone to clogging (trends with only 3 representative fiber-wettability are shown for clarity). (B) The resulting maximum achievable aerodynamic efficiency for *clog-proof* square meshes as a function of fiber diameter for different fiber wettabilities.

Therefore, from the results we conclude that *clog-proof* meshes with lower fiber diameters results in lower aerodynamic efficiency and provides greater impedance to the flow of fog and vice versa. Furthermore, variation of the fog-mesh fiber wettability was also seen to have a considerable impact on the design and resulting aerodynamics of *clog-proof* meshes. While it might be *wrongly* inferred here that clog proof meshes with larger fiber diameters are best suited for fog harvesting, this is not always true as the effect of deposition efficiency must be taken into consideration before commenting on the overall mesh efficiency.

3.3.2 Deposition and total efficiencies

Having established a high aerodynamic efficiency is not the only precondition of high overall capture efficiency. The fog droplets should also have a high deposition rate (and deposition efficiency) on the fiber meshes. Langmuir and Blodgett [46] in their seminal work developed a correlation for deposition of small droplets headed towards an infinitely long cylinder, thereby demonstrating the effects of the inertial and viscous forces. The capture efficiency of such a fog particle from a flow field is determined by its Stokes number (St), defined as the ratio of the characteristic time of the particle (t_p) to the characteristic time of flow (t_f) around the collector (herein, a smooth cylindrical fog-mesh fiber element). The stopping time of the particle is conventionally computed using Stokes linear drag law and in such reversible Stokesian flow regimes wherein the inertial forces are small and the particles can be assumed to be perfect solid spheres, the drag force on a fog particle can be estimated as $F_D = 6\pi R_{fog}\mu_{air}u$, where R_{fog} is the radius of the fog particle, ρ_{fog} the density of fog water, μ_{air} the dynamic viscosity and u the flow velocity of the carrier medium (herein air), respectively. For a particle moving initially with the free stream velocity, the deceleration can therefore be simply estimated from Newton's second law as

$$a = \frac{F_D}{m} = \frac{6\pi R_{fog}\mu_{air}u}{(4/3)\pi R_{fog}^3\rho_{fog}} = \frac{9\mu_{air}u}{2R_{fog}^2\rho_{fog}} \quad (15)$$

The characteristic stopping time (t_p) after which the fog particle gets deposited on the fiber, may be estimated by momentum balance of a fog particle, such that,

$$t_p = \frac{u}{a} = \frac{2R_{fog}^2\rho_{fog}}{9\mu_{air}} \quad (16)$$

The characteristic time of flow (t_f) can be defined as the ratio of the length scale of the fog flow around a mesh fiber to the velocity of the free stream ($t_f = 2r_f/u$). Plugging the values for the characteristic times, the Stokes number (St) can be represented in terms of the mesh fiber Reynolds number ($Re_{fiber} = \rho_{air}u_{slip}(2r_f)/\mu_{air}$) as

$$St = \frac{2}{9}Re_{fiber} \frac{\rho_{fog}}{\rho_{air}} \left(\frac{R_{fog}}{2r_f}\right)^2 \quad (17)$$

The fog droplet deposition efficiency (η_d) for millimeter sized mesh-pores can be calculated directly by using the empirical expression that is widely acceptable in the literature [2, 46, 47] as

$$\eta_d = \frac{St}{(\pi/2)+St} \quad (18)$$

However, such estimation of deposition efficiency is limited only to very low fog particle Reynolds number, defined as $Re_{fog} = 2\rho_{air}uR_{fog}/\mu_{air}$. The average fog droplet diameter ($2R_{fog}$) and has been assumed to be $\sim 5 \mu\text{m}$ throughout the remainder of this study [2]. The estimation of deposition efficiencies at higher Re_{fog} , calls for the definition of a generalized Stokes number (St_g). Similar proposition for a generalized St had been earlier put forth by Israel and Rosner [48], to account for any non-Stokesian drag on a particle in a stream. According to the revised analysis (see ESI S2.0 for the derivation), the deposition efficiency η_d may be expressed in terms of the generalized Stokes number St_g as

$$\eta_d^{-1} \cong 1 + 1.25 \left(St_g - \frac{1}{8}\right)^{-1} - 1.4 \times 10^{-2} \left(St_g - \frac{1}{8}\right)^{-2} - 0.508 \times 10^{-4} \left(St_g - \frac{1}{8}\right)^{-3} \quad (19)$$

for $St_g > 0.14$. Thus, for all our fog deposition efficiency estimations, we resort to using the Israel and Rosner generalized deposition efficiency (Equation 19) for any $St_g > 0.14$, while using the Langmuir-Blodgett [46] equations with St_g (Equation 18) for $St_g \leq 0.14$. Figure 9A plots the different deposition efficiencies for variations in fiber radii for different realistic sets of fog free-stream velocities ranging up to 10 m/s. A higher fog stream velocity is seen to result in a higher inertial deposition of the fog droplets, thereby leading to an increase in the deposition efficiency for all fiber diameters (Figure 9A). However, smaller fiber diameter result in better deposition than that observed on larger ones. This may be attributed to the fact that a slender fiber gives rise to a sharper deviation of the streamlines as the flow encounters it, leading to a larger inertial effect as the particles attempt to flow past the fibers. For further characterization of overall efficiencies of the *clog-proof* meshes, a free fog stream flow velocity of 5 m/s is chosen, since it is typical in industrial cooling tower fog harvesting applications.

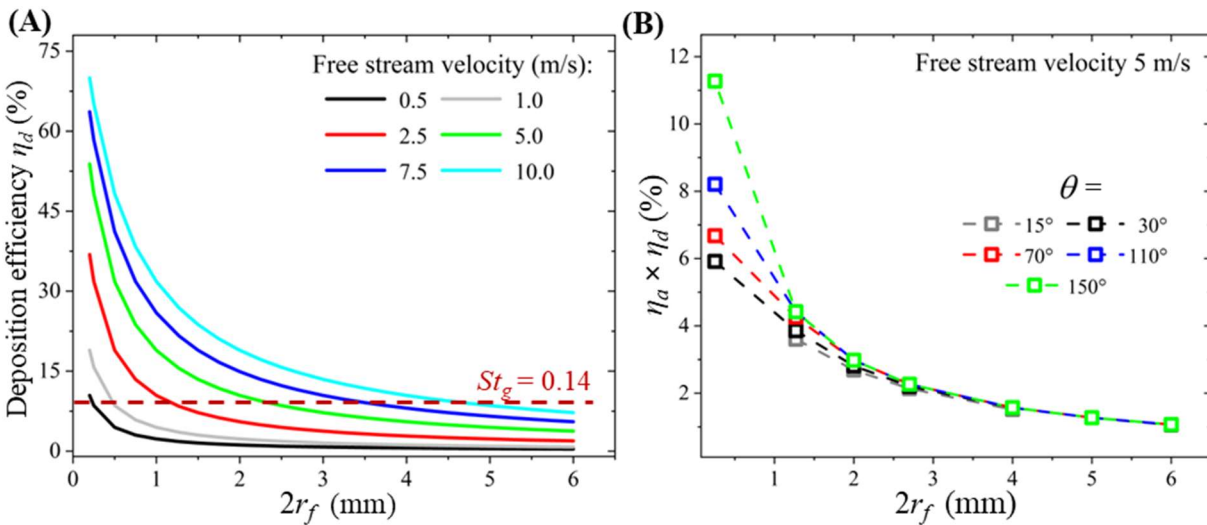


Figure 9: (A) Variation of deposition efficiencies (η_d) as function of fiber diameters at different fog flow velocities as evaluated from Equation 18 for $St_g \leq 0.14$ and from Equation 19 for $St_g > 0.14$. η_d resulting from $St_g = 0.14$ has been marked with a dashed red line. (B) Variation of ($\eta_d \times \eta_a$) at different optimal *clog-proof* shade coefficients for different mesh fiber diameters and wettability conditions. Total efficiencies have been estimated for a representative fog flow velocity of 5 m/s.

Reckoning the optimum shade coefficients pertaining to the maximum aerodynamic efficiency for design of *clog-proof* meshes corresponding to their wettability and fiber diameters (Figure 6B) and the deposition efficiencies from Figure 9A are combined to deduce the overall efficiency $\eta_d \times \eta_a$ of the *clog-proof* fog harvesters, which is reported in Figure 9B. The overall product of aerodynamic and deposition efficiencies is observed to decrease with increase in fiber diameters for designed *clog-proof* meshes. This decrease in the overall efficiency is in stark contrast to variation of aerodynamic efficiency with fiber diameter variation. As can be understood from the variation of both the efficiencies, deposition efficiency plays a stronger role and dominates to determine the final trend of the overall efficiency. Although, there is an increase in aerodynamic efficiency with increasing fiber radii (as discussed in the last section), this is not sufficient to compensate for the decrease in deposition efficiency. It is also noted that for fiber radii below ~ 2.7 mm (the capillary length-scale of water), the fog collection efficiency improves with increased hydrophobicity of the fiber, while retaining the *clog-proof* of the mesh. However,

for larger mesh fiber diameter, the mesh fiber wettability is found to play very little role. This arises from the fact that the maximum achievable η_a of the *clog-proof* design of the mesh became almost insensitive to the mesh wettability for fiber diameter exceeding ~ 2.7 mm.

The article provides the basis for the design of a fog harvesting mesh that estimates the optimal mesh pitch for a combination of mesh fiber diameter and the fiber wettability to ensure clog-free operation and maximizes the overall collection efficiency. While thin hydrophobic fibers are found perform efficiently due to high deposition efficiencies in optimal *SC clog-proof* designs, it is important to keep in mind that they tend to suffer from re-entrainment and premature drainage in fog harvesting applications [31]. Incorporation of drainage efficiencies and re-entrainment factors to better realize such *clog-proof* meshes, remains a future direction. Although the current study does not take into consideration the events of premature dripping and flow-induced re-entrainment, it attempts to ameliorate the occurrence of mesh clogging, which is a major component attributing to the fog harvester performance degradation during field deployment.

4 Conclusions

We have investigated the development of a *clog-free* mesh design by incorporating droplet morphology maximal parameters (H_{max} or W_{max}) into the geometry of fog harvesting meshes. Although numerous forms of deposited droplet configurations can exist on the mesh, we have simplified our problem by deconstructing the mesh and looking at the droplet growth and interaction on a single smooth cylindrical horizontal mesh fiber. First, the quasi-static growth and morphology evolution of a water droplet on a cylindrical fiber of given diameter and surface wettability has been investigated experimentally and through Surface Evolver simulations. The maximal height and spread of the droplets, as they hang from the horizontal fiber, until they grow large enough to be shed by gravity, are noted, and used to estimate the minimum mesh pitch that would ensure clog-free operation. The estimated minimum mesh pitch is then used to specify minimum shade coefficients (*SC*) of square mesh pore fog harvesters. This optimal *SC* is further used to calculate aerodynamic, deposition, and overall mesh efficiencies in typical industrial scale cooling tower fog harvesting applications. We find that for fog harvesting meshes designed at the *clog-proof* condition, hydrophobic fibers ($\theta > 90^\circ$) with diameters below the capillary length scale, outperform other fibers in terms of overall efficiency. For *clog-proof* meshes with fiber diameters above the capillary length scale, mesh wettability is seen to play very little role in determining the overall efficiency. Further the overall efficiency is seen to decrease with increase of fiber diameter. Such a trend can be attributed to the fact that the optimally-designed *clog-proof* meshes, with a square pore, have a constant aerodynamic efficiency corresponding to an optimal *SC* of 0.52 at larger diameters and the trend in overall efficiency is directly influenced by the decreasing deposition efficiency of larger fibers.

5 Acknowledgement

Authors gratefully acknowledge the funding from DST-SERB, India through Project No. CRG/2019/005887. AM thankfully acknowledge the assistantship from JU-RUSA. Help from Rupam Mahanta in editing of the *ESI* videos is also gratefully acknowledged.

6 Declaration of competing interests

AM, AD, AD and RG are the inventors on a patent application titled “Never-clog’ mesh designs for capture and separation of a dispersed phase from a flowing fluid stream and systems thereof”

related to this work filed with Indian patent office (application no: 202231045629, filed on 10th August 2022).

7 References

- [1] Connor, R. (2015). The United Nations world water development report 2015: water for a sustainable world (Vol. 1). UNESCO publishing.
- [2] Park, K. C., Chhatre, S. S., Srinivasan, S., Cohen, R. E., & McKinley, G. H. (2013). Optimal design of permeable fiber network structures for fog harvesting. *Langmuir*, 29(43), 13269-13277.
- [3] Ghosh, R., Ray, T. K., & Ganguly, R. (2015). Cooling tower fog harvesting in power plants—A pilot study. *Energy*, 89, 1018-1028.
- [4] Stechkina, I. B., Kirsch, A. A., & Fuchs, N. A. (1969). Studies on fibrous aerosol filters—iv calculation of aerosol deposition in model filters in the range of maximum penetration. *Annals of Occupational Hygiene*, 12(1), 1-8.
- [5] Lee, J., So, J., Bae, W. G., & Won, Y. (2020). The design of hydrophilic nanochannel-macrostripe fog collector: Enabling wicking-assisted vertical liquid delivery for the enhancement in fog collection efficiency. *Advanced Materials Interfaces*, 7(11), 1902150.
- [6] Datta, A., Mukhopadhyay, A., Dutta, P. S., Saha, A., Datta, A., & Ganguly, R. (2021, December). Droplet detachment from a horizontal fiber of a fog harvesting mesh. In *Conference on Fluid Mechanics and Fluid Power* (pp. 485-490). Singapore: Springer Nature Singapore..
- [7] Ghosh, R., & Ganguly, R. (2018). Harvesting water from natural and industrial fogs—opportunities and challenges. *Droplet and spray transport: paradigms and applications*, 237-266.
- [8] Gilet, T., Terwagne, D., & Vandewalle, N. (2010). Droplets sliding on fibres. *The European Physical Journal E*, 31, 253-262.
- [9] Shi, W., Anderson, M. J., Tulkoff, J. B., Kennedy, B. S., & Boreyko, J. B. (2018). Fog harvesting with harps. *ACS Applied Materials & Interfaces*, 10(14), 11979-11986.
- [10] Shi, W., van der Sloot, T. W., Hart, B. J., Kennedy, B. S., & Boreyko, J. B. (2020). Harps enable water harvesting under light fog conditions. *Advanced Sustainable Systems*, 4(6), 2000040.
- [11] Goswami, S., Sidhpuria, R. M., & Khandekar, S. (2023). Effect of Droplet-Laden Fibers on Aerodynamics of Fog Collection on Vertical Fiber Arrays. *Langmuir*.
- [12] Shi, W., De Koninck, L. H., Hart, B. J., Kowalski, N. G., Fugaro, A. P., van der Sloot, T. W., ... & Boreyko, J. B. (2020). Harps under heavy fog conditions: superior to meshes but prone to tangling. *ACS Applied Materials & Interfaces*, 12(42), 48124-48132.
- [13] Weyer, F., Duchesne, A., & Vandewalle, N. (2017). Switching behavior of droplets crossing nodes on a fiber network. *Scientific Reports*, 7(1), 13309.
- [14] Adam, N. K. (1937). Detergent action and its relation to wetting and emulsification. *Journal of the Society of Dyers and Colourists*, 53(4), 121-129.
- [15] Eral, H. B., de Ruitter, J., de Ruitter, R., Oh, J. M., Semprebon, C., Brinkmann, M., & Mugele, F. (2011). Drops on functional fibers: from barrels to clamshells and back. *Soft Matter*, 7(11), 5138-5143.
- [16] Carroll, B. J. (1976). The accurate measurement of contact angle, phase contact areas, drop volume, and Laplace excess pressure in drop-on-fiber systems. *Journal of colloid and interface science*, 57(3), 488-495.
- [17] McHale, G., Newton, M. I., & Carroll, B. J. (2001). The shape and stability of small liquid drops on fibers. *Oil & Gas science and technology*, 56(1), 47-54.
- [18] Sarkar, S., Gukeh, M. J., Roy, T., Gaikwad, H., Bellussi, F. M., Moitra, S., & Megaridis, C. M. (2023). A new methodology for measuring solid/liquid interfacial energy. *Journal of Colloid and Interface Science*, 633, 800-807.
- [19] Berthier, J., Brakke, K. A., & Berthier, E. (2016). *Open microfluidics*. John Wiley & Sons.

- [20] Chou, T. H., Hong, S. J., Liang, Y. E., Tsao, H. K., & Sheng, Y. J. (2011). Equilibrium phase diagram of drop-on-fiber: coexistent states and gravity effect. *Langmuir*, 27(7), 3685-3692.
- [21] Brakke, K. A. (1992). The surface evolver. *Experimental mathematics*, 1(2), 141-165.
- [22] Ang, B. T. W., Zhang, J., Lin, G. J., Wang, H., Lee, W. S. V., & Xue, J. (2019). Enhancing water harvesting through the cascading effect. *ACS applied materials & interfaces*, 11(30), 27464-27469.
- [23] Park, J. K., & Kim, S. (2019). Three-dimensionally structured flexible fog harvesting surfaces inspired by Namib Desert Beetles. *Micromachines*, 10(3), 201.
- [24] Raut, H. K., Ranganath, A. S., Baji, A., & Wood, K. L. (2019). Bio-inspired hierarchical topography for texture driven fog harvesting. *Applied Surface Science*, 465, 362-368.
- [25] Zhang, L., Wu, J., Hedhili, M. N., Yang, X., & Wang, P. (2015). Inkjet printing for direct micropatterning of a superhydrophobic surface: toward biomimetic fog harvesting surfaces. *Journal of Materials Chemistry A*, 3(6), 2844-2852.
- [26] Zhai, L., Berg, M. C., Cebeci, F. C., Kim, Y., Milwid, J. M., Rubner, M. F., & Cohen, R. E. (2006). Patterned superhydrophobic surfaces: toward a synthetic mimic of the Namib Desert beetle. *Nano Letters*, 6(6), 1213-1217.
- [27] Fessehaye, M., Abdul-Wahab, S. A., Savage, M. J., Kohler, T., Gherezghiher, T., & Hurni, H. (2014). Fog-water collection for community use. *Renewable and Sustainable Energy Reviews*, 29, 52-62.
- [28] Bhushan, B. (2020). Design of water harvesting towers and projections for water collection from fog and condensation. *Philosophical Transactions of the Royal Society A: Mathematical, Physical and Engineering Sciences*, 378(2167), 20190440.
- [29] Ghosh, R., & Ganguly, R. (2020). Fog harvesting from cooling towers using metal mesh: Effects of aerodynamic, deposition, and drainage efficiencies. *Proceedings of the Institution of Mechanical Engineers, Part A: Journal of Power and Energy*, 234(7), 994-1014.
- [30] Sontag, D. S., & Saylor, J. R. (2016). An experimental study of the collection of fog droplets using a mesh fabric: Possible application to cooling towers. *Journal of Energy Resources Technology*, 138(2), 024501.
- [31] Ghosh, R., Patra, C., Singh, P., Ganguly, R., Sahu, R. P., Zhitomirsky, I., & Puri, I. K. (2020). Influence of metal mesh wettability on fog harvesting in industrial cooling towers. *Applied Thermal Engineering*, 181, 115963.
- [32] Amrei, M. M., Venkateshan, D. G., D'Souza, N., Atulasimha, J., & Tafreshi, H. V. (2016). Novel approach to measuring the droplet detachment force from fibers. *Langmuir*, 32(50), 13333-13339.
- [33] Sarkar, S., Roy, T., Roy, A., Moitra, S., Ganguly, R., & Megaridis, C. M. (2021). Revisiting the supplementary relationship of dynamic contact angles measured by sessile-droplet and captive-bubble methods: Role of surface roughness. *Journal of Colloid and Interface Science*, 581, 690-697.
- [34] Das, C., Gupta, R., Halder, S., Datta, A., & Ganguly, R. (2021). Filmwise condensation from humid air on a vertical superhydrophilic surface: Explicit roles of the humidity ratio difference and the degree of subcooling. *Journal of Heat Transfer*, 143(6).
- [35] Zhou, F., Zhuang, D., Lu, T., & Ding, G. (2020). Observation and modeling of droplet shape on metal fiber with gravity effect. *International Journal of Heat and Mass Transfer*, 161, 120294.
- [36] Hu, H., Lai, Z., & Hu, C. (2023). Droplet shedding characteristics on metal fibers with different wettability and inclined angles. *International Journal of Refrigeration*, 130, 271-277.
- [37] Young, T. (1805) An essay on the cohesion of fluids. *Philosophical Transactions*,; 95: 65-87
- [38] Gennes, P. G., Brochard-Wyart, F., & Quéré, D. (2004). *Capillarity and wetting phenomena: drops, bubbles, pearls, waves* (pp. p7-p9). Springer New York.
- [39] Ray, S., & Ganguly, R. (2020). Evolution of nanoliter size fluid droplet on micropatterned surface. *Sādhanā*, 45(1), 1-10.
- [40] Carroll, B. J. (1986). Equilibrium conformations of liquid drops on thin cylinders under forces of capillarity. A theory for the roll-up process. *Langmuir*, 2(2), 248-250.

- [41] Law, B. M., McBride, S. P., Wang, J. Y., Wi, H. S., Paneru, G., Betelu, S., ... & Aratono, M. (2017). Line tension and its influence on droplets and particles at surfaces. *Progress in surface science*, 92(1), 1-39.
- [42] Koo, J.-K., & James, D. F. (1973). Fluid flow around and through a screen. *Journal of Fluid Mechanics*, 60(03), 513.
- [43] Steiros, K., & Hultmark, M. (2018). Drag on flat plates of arbitrary porosity. *Journal of Fluid Mechanics*, 853.
- [44] de Dios Rivera, J. (2011). Aerodynamic collection efficiency of fog water collectors. *Atmospheric Research*, 102(3), 335-342.
- [45] Azeem, M., Guérin, A., Dumais, T., Caminos, L., Goldstein, R. E., Pesci, A. I., ... & Dumais, J. (2020). Optimal design of multilayer fog collectors. *ACS applied materials & interfaces*, 12(6), 7736-7743.
- [46] Langmuir, I., & Blodgett, K. (1946). A mathematical investigation of water droplet trajectories (No. 5418). Army Air Forces Headquarters, Air Technical Service Command.
- [47] Shahrokhian, A., Feng, J., & King, H. (2020). Surface morphology enhances deposition efficiency in biomimetic, wind-driven fog collection. *Journal of the Royal Society Interface*, 17(166), 20200038.
- [48] Israel, R., & Rosner, D. E. (1982). Use of a generalized Stokes number to determine the aerodynamic capture efficiency of non-Stokesian particles from a compressible gas flow. *Aerosol Science and Technology*, 2(1), 45-51.